95-GT-370

CASCADE VORTICAL GUST RESPONSE INCLUDING STEADY LOADING EFFECTS

Gregory H. Henderson*

School of Mechanical Engineering

Purdue University

West Lafayette, Indiana

Sanford Fleeter

School of Mechanical Engineering

Purdue University

West Lafayette, Indiana

ABSTRACT

A series of experiments are performed to investigate the
effect of steady loading and separated flow on the unsteady
vortical gust response of both low and high solidity blade
rows, including the effects of airfoil camber. This is
accomplished utilizing a unique single stage turbomachine
research facility in which the flow is not generated by the
blading but rather by an additional fan. This provides the
ability to quantify the steady or mean performance of the stator
row over a range of steady loading levels both with and
without unsteady flow effects. In particular, for a particular
mean stator angle-of-attack, the steady and mean aerodynamic
performance are determined in a steady flow and also in an
unsteady flow generated by a rotor composed of perforated
plates at the same mean operating condition. This enables the
stator vane row dynamic stall conditions to be identified. The
unsteady aerodynamic response of both symmetric and
cambered stator vanes configured as low and high solidity
stator vane rows is then investigated over a range of mean
angle-of-attack values, including attached and separated flows
with dynamic stall.

NOMENCLATURE

C	airfoil chord
C_L	lift coefficient
C_p	surface pressure coefficient
$C_{\Delta P}$	differential pressure coefficient
k_c	reduced frequency based on chord
N_h	number of harmonics
P	perturbation pressure
S	vane spacing
$\overline{U}$	mean absolute velocity
$\hat{v}$	transverse gust component

w_{rms}	velocity scale factor (velocity fluctuation root-mean-square)
α	angle-of-attack
ρ	density
overbar	mean component
$\wedge$	harmonic component
subscripts	
l	lower surface
u	upper surface
2	rotor exit

INTRODUCTION

Advanced blade rows are designed to operate with high
steady loading to meet performance requirements. As a result,
the flow may separate from the suction surface, particularly
when the engine is accelerating or operating near the surge
line in a high output situation. This suction surface flow
separation may have a significant effect on the aeromechanics
of the blade row, both forced response and flutter. In fact, the
majority of forced response resonance conditions indicated on
Campbell diagrams are at off-design conditions where flow
separation may exist. Also, stall flutter is still an important
design consideration and development problem. However, the
effects of high steady loading and separated flow on the
resulting unsteady aerodynamic blade row response are
relatively unstudied.

With regard to steady loading and separated flow, it is well
known for isolated airfoils that dynamic stall has significant
effects, delaying the onset of stall to higher mean angles of
attack and loading levels. This enables an airfoil to operate
without flow separation at mean angles-of-attack greater than
steady stalling. Dynamic stall generally refers to the unsteady
separation of the flow from the upper surface of an airfoil and
the stall phenomena of the airfoil oscillating into and out of
steady stall. It begins at an angle-of-attack greater than the
static stall angle, i.e., the oscillation of the airfoil and the

---

* Advanced Product Development
  Cummins Engine Company. Columbus. Indiana

associated unsteady flow delay the onset of stall. Thus an oscillating airfoil can reach higher angles-of-attack than a static airfoil before the flow separates. The predominant feature of dynamic stall is the shedding of a strong vortex-like disturbance from the airfoil leading edge region. This vortex moves downstream over the airfoil upper surface of an isolated airfoil at about 35% to 40% of the free stream velocity. The formation and movement of the vortex depends on the airfoil shape, angle-of-attack and its rate of change. The airfoil remains stalled until the angle-of-attack drops sufficiently for the flow to reattach, generally occurring at an angle less than the static stall angle. The dynamic stall phenomenon and its effects vary depending on the airfoil shape, reduced frequency, mean angle and amplitude of oscillation, Mach number, Reynolds number, type of airfoil motion, sweep, and three dimensional flow effects.

Dynamic stall events, namely separation of the flow, formation of the vortex, movement of the vortex, and reattachment, take a finite time to develop. However, once the flow is separated, the dynamic stall events introduce two important physical consequences. The first is the hysteresis produced by the lag and asymmetry of the unsteady aerodynamic forces with respect to the airfoil motion. During dynamic stall, isolated airfoils exhibit large hysteresis loops in both lift and pitching moment as a function of the airfoil angle-of-attack $\overline{\alpha}$. Hence an airfoil with positive $\dot{\alpha}$ stalls at an angle greater than the steady or static stall angle α_{steady}, termed stall delay, while the stall recovery during negative $\dot{\alpha}$ occurs at an angle-of-attack less than α_{steady}. This is in contrast to the steady or quasi-steady case where no hysteresis is produced since the flow field adjusts immediately to each change in angle-of-attack.

The second consequence of dynamic stall is aerodynamic damping. With regard to blade row aerodynamically forced vibrations, aerodynamic damping is critical, limiting the maximum response. When the aerodynamic damping is negative, the airfoil extracts energy from the flow, resulting in flutter. Stall flutter, resulting from this negative damping, tends to occur when the airfoil is oscillating into and out of stall. The pitching moment coefficient variation with the angle-of-attack are loops which correspond to negative and positive aerodynamic damping, with a net negative damping resulting in divergent oscillations or stall flutter.

Although of research importance and interest for isolated airfoils, for example McCroskey [1981], dynamic stall has not been addressed in turbomachines. This is not because dynamic stall may not be significant in turbomachines at high loading conditions, but rather because of the differences between isolated airfoil and turbomachine blade row unsteady flow phenomena. Also, the experimental facilities utilized for turbomachinery research, i.e., research compressors and turbines and wind tunnels, are not conducive to investigating dynamic stall of turbomachine blading. In contrast to isolated airfoils where the flow is steady with the flow unsteadiness generated by the airfoil motion, the flow is inherently unsteady in turbomachine blade rows. Namely the wakes from upstream blade and vane rows are the primary source of the unsteady aerodynamics of downstream blade rows. This inherent unsteady flow can delay the onset of flow separation

of turbomachine blading at high loading conditions, i.e., dynamic stall occurs in turbomachine blade rows at high mean angle-of-attack values. However, other than prop-fan applications, Reddy and Mehmed [1989], there has been minimal research applied to dynamic stall of turbomachine blade rows.

Experimentally it is necessary to model the basic unsteady aerodynamic phenomena inherent in this time variant interaction, including the mean angle-of-attack, velocity and pressure variations, aerodynamic forcing function waveforms, reduced frequency, and blade row interactions. As a result, turbomachine experiments are typically performed in research compressors and turbines, with the steady and unsteady flow generated by the rotor blades. The effect of steady loading is considered by varying the operating conditions along a constant speed line. Thus, experimentally the steady stall angle-of-attack is not determined, with the high loading operation terminating when the surge line or a stall flutter condition is encountered. In this regard, Henderson and Fleeter [1994] investigated the effect of stall for very low solidity symmetric airfoils.

This paper addresses the effect of turbomachine blade row steady loading and separated flow, including dynamic stall effects, on the resulting gust response of both low and high solidity uncambered and cambered blade rows. This is accomplished utilizing a unique single stage turbomachine research facility in which the flow is not generated by the blading but rather by an additional fan. This provides the ability to quantify the steady or mean performance of the stator row over a range of steady loading levels or mean angle-of-attack values both with and without unsteady flow effects. In particular, for a specific stator mean angle-of-attack, the steady and mean stator aerodynamic performance are determined in a steady flow and also in an unsteady flow generated by a rotor composed of perforated plates at the same mean operating condition. This enables the stator vane row dynamic stall conditions to be identified. The unsteady aerodynamic response of both symmetric and cambered vanes configured as low and high solidity vane rows is then investigated over a range of mean angles of attack.

RESEARCH FACILITY

The Purdue Annular Cascade Research Facility is an open-loop draw-through type wind tunnel capable of test section velocities of 70 m/sec (220 ft/sec). The inlet flow, conditioned first by a honeycomb section and then a settling chamber, accelerates into the annular test section via a bellmouth inlet. The test section exit flow is diffused into a large plenum. The 224 kW (300 hp) centrifugal fan located downstream of the plenum draws the air through the facility, with guide vanes at the fan inlet allowing flow rate adjustment through the facility. The annular test section, Figure 1, houses a rotor independently driven by a 7.5 kW (10 hp) A-C motor controlled by a variable frequency drive. The rotor creates the desired unsteady flow field to the downstream stator row. The separate drive motors on the rotor and system fan uncouple the rotor speed from the through-flow velocity, thereby providing independent control over the unsteady aerodynamic parameters. For these experiments, the unsteady periodic flow to the stator vane row is generated by a rotor comprised of perforated plates, Figure 1, fabricated from 56% porosity

aluminum sheet and mounted on the rotor such that the plate width is normal to the rotor axis. This results in a dominant vortical wake forcing function to the downstream vane row.

Symmetric and cambered airfoil stator airfoils, Figure 2, are utilized in low and high solidity configurations. The airfoil chord and span are both 0.152 m (6.0 in.). The twelve midspan chordwise tap locations provide highly detailed spatial resolution of the midspan chordwise pressure distributions. The stator airfoils are mounted through holes in the outer diameter of the test section by trunnions attached at the 35% chord. The stator airfoil stagger angle can be set to within ± 0.5°. The C/S ≈ 0.17 low-solidity stator cascade is comprised of the four instrumented airfoils, two static and two dynamic. The C/S = 0.78 high-solidity stator cascade is comprised of eighteen airfoils

DATA ACQUISITION & ANALYSIS

Both steady and unsteady data are required for these experiments. The steady data define the steady or mean flow performance of the stator vane row. The unsteady data define the perforated plate rotor generated forcing function or gust specified by the unsteady velocity and static pressure fluctuations downstream of the rotor, as well as the resulting unsteady gust response of the stator vane row.

All time variant signals are digitized over one rotor revolution using approximately 2,000 samples. The number of ensemble averages necessary to obtain clean periodic time traces was investigated. Ensemble averaging the hot-wire and pressure transducer signals 150 and 100 times, respectively, produces very clean periodic time traces with the random fluctuations averaged away. The Fourier components of the ensemble averaged time traces are numerically determined with Fast Fourier Transform software. The sample frequency is set and the number of samples is adjusted to produce time records of exactly one rotor rotation period to eliminate frequency leakage problems in Fourier Transform analysis. The sample frequency and number of digitizations are set based upon an accurate rotor rotational speed. The rotor rotational speed is measured by digitizing the shaft trigger signal at the maximum sample frequency and counting the number of samples between shaft triggers.

Stator Vane Steady & Unsteady Performance

The stator vane surface steady data are nondimensionalized as a steady surface pressure coefficient, with a steady differential pressure coefficient then determined.

$$\overline{C}_p(x) = \frac{\overline{p}(x) - p_\infty}{\frac{1}{2}\rho\overline{U}^2} \qquad \overline{C}_{\Delta p} = \overline{C}_{p,l} - \overline{C}_{p,u} \qquad (1)$$

where $\overline{p}$ is the time-averaged airfoil surface pressure, p_∞ is the free stream pressure measured on the test-section outer diameter just upstream of the stator cascade, and the subscripts l and u refer to the lower and upper airfoil surfaces.

The airfoil unsteady surface pressures are measured with PCB Piezotronics model 103A piezoelectric pressure transducers. The transducers have a nominal sensitivity of 0.22 mv/Pa (1,500 mv/psi) and a natural frequency of 13 kHz. After the

transducers were installed in the airfoil, the dynamic response of each airfoil transducer-passage system was experimentally determined to correct for any passage effects. These chordwise pressure response data are presented as nondimensional pressure coefficients and are correlated with a steady linear-theory analysis, Henderson and Fleeter [1994].. The unsteady response data are correlated with predictions from the compressible flow analysis of Smith [1972]. These analyses account for the cascade stagger angle and solidity, with Smith's unsteady analysis also considering the reduced frequency k_C and the interblade phase angle.

The unsteady periodic signals are Fourier decomposed, with each pressure harmonic nondimensionalized by calculating an unsteady surface pressure coefficient, and the harmonic differential coefficient determined.

$$\widehat{C}_p(x) = \frac{\widehat{p}(x)}{\rho\widehat{U}\widehat{v}} \qquad \widehat{C}_{\Delta p} = \widehat{C}_{p,l} - \widehat{C}_{p,u} \qquad (2)$$

where $\widehat{p}$ and $\widehat{v}$ denote the harmonic surface pressure and transverse gust component.

Direct comparison of the experimental and theoretical steady and unsteady lift and moment coefficients is accomplished by integrating the experimental and theoretical chordwise differential pressure coefficients over the airfoil chord.

$$C_L = \frac{1}{C}\int_{0.025C}^{0.95C} C_{\Delta p}\,dx \qquad (3)$$

The trapezoidal rule is used to evaluate the integrals from the discrete pressure coefficient data and the theoretical predictions. The differential pressure distributions are integrated from the leading edge tap location, 0.025C, to the trailing edge tap location, 0.95C.

The complex valued unsteady pressure coefficients, lift coefficients, and moment coefficients contain both amplitude and phase angle information. These quantities are referenced to the transverse gust sinusoid measured by the cross hot-wire on the airfoil leading edge plane. To obtain pressure coefficients for a single equivalent airfoil, the pressure signals are phase corrected to account for the circumferential locations of the instrumented airfoils. The uncertainty of the measured surface pressure coefficients is estimated at 10% where the response is large near the leading edge.

Rotor Generated Gust Forcing Function

The unsteady data defining the forcing function or gust generated by the rotating row of perforated plates are determined by the midspan unsteady velocity and static pressure fluctuations downstream of these rotors. The rotor-exit flow field unsteady total pressure is measured with a hemispherical-nosed total pressure pitot tube fitted with an unsteady pressure transducer. The amplitude of the incident flow angle is a function of the wake generator, with the angle of the pitot tube set to minimize flow angle variations for each wake generator. The criterion presented by Becker and Brown

3

[1974] shows that the errors produced by the incident flow angle fluctuations should be no more than 6%. A cross bot-wire anemometer is used to measure the unsteady velocity field. The absolute velocity magnitude and flow angle errors are estimated at 4% and 0.5° respectively. The wake velocity deficits are decomposed into streamwise and transverse velocity components, with the unsteady static pressure calculated as the difference between the unsteady total pressure and the unsteady dynamic pressure.

The unsteady velocity vector and static pressure measurements are scaled so that an unsteady velocity vector of unit length represents a velocity pressure fluctuation equal to a unit pressure fluctuation. The velocity and static pressure scale factors, w_{rms} and p_{rms} for small perturbations are linearly related by

$$p_{rms} = \rho \overline{U}_2 w_{rms} \qquad (4)$$

where w_{rms} is the root-mean-square of the velocity fluctuations and p_{rms} is calculated from Equation 4. Since w_{rms} and p_{rms} are linearly related by the constant $\rho \overline{U}_2$, scaling in this manner allows the direct determination of the relative proportions of the velocity and static pressure fluctuations.

RESULTS

A series of experiments are performed to investigate the effect of steady loading, i.e., vane angle-of-attack, and separated flow including dynamic stall on the resulting unsteady aerodynamic stator vane row response of both low and high solidity symmetric and cambered airfoil cascades. For a particular stator angle-of-attack, the steady and mean stator aerodynamic performance are determined in a steady flow and also in an unsteady flow generated by a rotor at the same mean operating condition,. This identifies the stator vane row dynamic stall conditions. The rotor is comprised of twenty perforated plate wake generators, corresponding to a reduced frequency of approximately 1.35 based on semichord. The unsteady aerodynamic response of the vane rows are then investigated over a range of mean angles of attack. Note that the pressure data are nondimensionalized by the velocity data obtained with the stator airfoils removed.

Gust Forcing Function

The perforated-plate rotor generated aerodynamic forcing function to the downstream vane row is presented in Figure 3. No stator vanes were installed for these measurements. The periodic velocity vector profile and static pressure distribution define the forcing function. A complete forcing function composed of N_h harmonics is shown together with the forcing function fundamental harmonic.

There is a negligible potential field. The viscous effects within the wake diffuse quite rapidly, leaving a large velocity deficit with a negligible static pressure perturbation. Hence, the perforated plate rotor generates a dominantly vortical gust forcing function, indicated by the minimal unsteady static pressure field. Note that the measured static pressure perturbation is non-zero near the edges of each wake. It is believed that this is a measurement artifact due, in part, to the

combination of a rapidly changing instantaneous flow angle at the edge of the perforated plate gust and the angular sensitivity of the total pressure probe.

Steady & Time-Averaged Cascade Loading

The effect of unsteady flow on the time-averaged vane loading is determined by measuring the surface pressure distributions in a steady flow field with no rotor and the time-averaged airfoil surface pressure distributions in the rotor generated unsteady flow.

Low Solidity Cascade

The steady, i.e. no rotor wake generators, and time-averaged lift coefficients for the low-solidity symmetric and cambered stator cascades are presented as a function of the angle-of-attack in Figure 4.

For the symmetric-airfoil, the steady lift coefficients correlate well with the steady predictions and each other for mean angles-of-attack $10° \geq \overline{\alpha} \geq -10°$. For $|\overline{\alpha}| > 10°$, the steady lift data and prediction deviate. The steady lift decrease with angle-of-attack for $\overline{\alpha} > 15°$, indicative of steady stall. In contrast, the unsteady flow has noticeable effects on the time-averaged lift, i.e., with the wake generators. First, the time-averaged lift and corresponding steady predictions have somewhat different slopes for $7.5° \geq \overline{\alpha} \geq -12°$, with the time-averaged lift slightly increased over the steady lift, i.e., the unsteady flow results in increased time-averaged lift as compared to the steady lift. The slope of the steady lift begins to decrease for $\overline{\alpha}$ between 7.5° and 10°, with the time-averaged lift decreasing for $\overline{\alpha} > 17.5°$. This ability of the time averaged lift to increase with angle-of-attack beyond the steady stall angle is clearly an unsteady flow effect which will be shown to be associated with dynamic stall. It should also be noted that similar trends are apparent at large negative angles-of-attack, i.e., the steady and time-averaged lift curves change slope, with the steady lift falling off before the time-averaged lift. However, the large positive and negative angle-of-attack results are dissimilar even though the airfoils are symmetric.

For the cambered stators, the predicted lift variation is offset to higher angle-of-attack values than the symmetric lift curve due to the additional lift of the airfoil camber, although the predicted lift curve slope is the same for both airfoil profiles. The cambered-airfoil steady lift has the same slope as the prediction but is slightly lower in value for $7.5° \geq \overline{\alpha} \geq -10°$. The steady lift and prediction then deviate from one another, with the steady lift being substantially decreased, indicating steady stall. Again the unsteady flow has important effects on the time-averaged lift. Namely, the time-averaged lift curve has a slightly increased slope as compared to the steady prediction or the steady data, with the time-averaged lift increased in value. Also, the onset of stall is delayed to higher angles-of-attack, with the time-averaged lift slope changing for $\overline{\alpha}$ between 12.5° and 15°. Again, the large positive and negative angle-of-attack results are dissimilar.

High Solidity Cascade

The steady and time-averaged lift coefficients for the high-solidity symmetric airfoil stator cascade are presented in Figure 5. Increasing the cascade solidity greatly reduces the

slope of the lift coefficient, demonstrating that individual airfoils in a high-solidity cascade are loaded less than airfoils in a low-solidity cascade at the same $\overline{\alpha}$. The steady lift data is in excellent agreement with the steady prediction over the complete mean angle-of-attack range. The unsteady flow again results in the time-averaged lift having a slightly different slope than the steady lift, with the time-averaged lift larger for positive angles-of-attack and smaller for negative angles-of-attack. Also, the time-averaged lift slope begins to change for $\overline{\alpha}$ between 17.5° and 22.5°, with the time-averaged lift decreased from the prediction at $\overline{\alpha} = 22.5°$.

Separation & Onset of Stall Delay

The steady airfoil surface pressure distributions reveal evidence of flow separation on the suction surfaces, with a region of constant pressure near the leading edge. This is explained by the presence of a separation bubble which appears at high angles-of-attack, as depicted in Figure 6. Aft of the separation bubble, the flow reattaches as confirmed by the decreasing magnitudes of the suction-surface pressure.

The delay in the onset of stall in the unsteady flow is clearly seen in the time-averaged chordwise pressure coefficients. The suction surface pressure coefficients resemble unstalled patterns, i.e. monotonically increasing, to higher angles-of-attack in the unsteady flow field. For example, as illustrated in Figure 6 the symmetric-airfoil suction surface at $\alpha = -15°$ in the steady flow field depicts more evidence of stall than at $\alpha = -17.5°$ in the unsteady flow field, even though the steady-flow-field angle-of-attack is smaller.

Vane Row Gust Response

The low loading, $\overline{\alpha} = 2.5°$, fundamental-harmonic unsteady chordwise pressure and pressure difference responses of the symmetric vanes, both low and high solidity, and the low solidity cambered vanes are presented in Figure 7. Note that for positive angles-of-attack, the suction surface is the upper surface. Also presented as a reference are the linear theory vortical gust predictions from Smith [1972]. Clearly, there is excellent correlation between the data and theory for low and high solidity symmetric airfoil configurations, both in magnitude and phase. The cambered airfoil data-theory correlation is not quite as good, attributed to the data being obtained with cambered airfoils whereas the prediction is for a flat plate airfoil cascade.

Loading Effects $\overline{\alpha} > 0$

For the low solidity symmetric airfoil vane row, the effect of steady loading. i.e. angle-of-attack, on the unsteady fundamental-harmonic unsteady chordwise pressure and pressure difference responses are presented for increasing positive angles-of-attack in Figure 8. Also included as a reference are the linear theory vortical gust predictions. The $\overline{\alpha} = 7.5°$ results are almost identical to those at $\overline{\alpha} = 2.5°$, both in terms of the unsteady pressure difference on the individual airfoil surfaces and the excellent correlation of the pressure difference data and the theory. However, further increases in the mean angle-of-attack has an important effect on the unsteady vane loading. At $\overline{\alpha} = 12.5°$, the magnitude of the upper surface unsteady pressure is significantly increased over the front portion of the airfoil, with the lower surface unsteady pressure magnitude essentially unchanged. As a result, the correlation of the pressure difference data and prediction

become relatively poor, particularly over the front portion of the airfoil. The upper surface phase angle chordwise distribution is also very interesting. Namely, a wave is apparent over the aft portion of the airfoil upper surface, indicated by the linear chordwise variation of the pressure phase angle. It should be recalled that for $|\overline{\alpha}| > 10$, the steady lift data and corresponding prediction deviate from one another, with the unsteady flow resulting in increased time-averaged lift as compared to the steady lift. Increasing the mean angle-of-attack to $\overline{\alpha} = 17.5°$ results in a further increase in the upper surface unsteady pressure magnitude, again with minimal effect on the lower surface, and, consequently even poorer correlation of the unsteady pressure difference data and the prediction. Also, the upper-surface unsteady response phase angle is dominated by an almost linear variation with chord, indicative of a wave propagating down the upper surface at approximately 50% of the free stream velocity.

With the low solidity cambered airfoil vane row, the effect of steady loading on the unsteady fundamental-harmonic unsteady chordwise pressure and pressure difference responses are presented for increasing positive angles-of-attack in Figure 9. The $\overline{\alpha} = 12.5°$ results are almost identical to those obtained at $\overline{\alpha} = 2.5°$, with the most apparent difference being the jump in the upper surface phase angle near the trailing edge. Also, the effects of the airfoil camber are apparent in the correlation of the data and the prediction. At $\overline{\alpha} = 17.5°$, the upper surface phase distribution corresponds to a wave phenomenon over most of the chord, and over the entire upper surface chord at $\overline{\alpha} = 22.5°$. This wave propagates down the upper suction surface at approximately 50% of the free stream velocity. Also, the upper surface unsteady pressure magnitude is greatly increased over the front portion of the chord, with the lower surface magnitude data relatively unaffected, at $\overline{\alpha} = 17.5°$ and 22.5°, with the larger effect at the higher mean angle-of-attack. This results in the decreased correlation between the data and the prediction at these very high mean angles of attack. Note that the steady and time-averaged lift showed that the unsteady flow delays the onset of stall, with the time-averaged lift slope changing for $\overline{\alpha}$ between 12.5° and 15°.

For the high solidity symmetric airfoil vane row, the effect of steady loading on the unsteady fundamental-harmonic unsteady chordwise pressure and pressure difference responses are presented for increasing positive angles-of-attack in Figure 10. At $\overline{\alpha} = 12.5°$, the results are nearly identical to those at $\overline{\alpha} = 2.5°$, an exception being the small decrease in the upper surface unsteady pressure magnitude very near to the leading edge. This results in a slight decrease in the excellence of the data - theory correlation in this region. This change in the upper surface unsteady pressure magnitude near the leading edge is somewhat increased at $\overline{\alpha} = 17.5°$. Also, there is evidence of wave propagation on the vane upper surface near the leading edge. These magnitude and phase effects result in decreased correlation between the unsteady pressure difference magnitude data and the theory near the leading edge, but excellent correlation over the rest of the chord. However, a further increase in the mean angle-of-attack to $\overline{\alpha} = 22.5°$ results in a large increase in the upper surface unsteady pressure magnitude over the front and mid-to-aft chord regions, with only minimal changes in the lower surface unsteady pressure

5

magnitude. Hence, the poor correlation of the unsteady pressure difference data and the prediction. Also, the upper-surface unsteady response phase angle is dominated by an almost linear variation with chord, indicative of a wave propagating down the upper airfoil surface. However, the propagating wave is being convected at approximately the free-stream velocity on the high solidity cascade suction surface, as compared to approximately 50% of the free stream velocity for the low solidity cascade.

Loading Effects $\overline{\alpha} < 0$

For the low solidity symmetric airfoil vane row, the effect of steady loading on the unsteady fundamental-harmonic unsteady chordwise pressure and pressure difference responses are presented for increasing negative angles-of-attack in Figures 11 and 12. Note that for negative angles-of-attack, the suction surface is now the lower surface. At $\overline{\alpha} = -2.5°$, the unsteady pressure difference data - theory correlation is excellent, both in terms of the unsteady pressure difference magnitude and phase, analogous to the $\overline{\alpha} = +2.5°$ results. Note that changing $\overline{\alpha}$ from positive to negative values reverses the surface with the larger unsteady pressure magnitude: for $\overline{\alpha} < 0°$, the lower surface has the larger unsteady pressure magnitude, whereas it was the upper surface for $\overline{\alpha} > 0°$ as expected. However, the upper and lower surface phase angles do not reverse, i.e., the same phase angle variation with chord is found on the upper and lower surfaces, independent of whether the mean angle-of-attack is positive or negative, even though the airfoils are symmetric.

Increasing $\overline{\alpha}$ to -7.5° affects the unsteady pressure magnitude near the leading edge, although the unsteady pressure difference magnitude data-theory correlation is still reasonable. However, a larger effect is apparent on the phase angle distribution. The upper surface, i.e., the pressure surface, exhibits a wave phenomenon, not the suction or lower surface as might have been expected. However, with a further decrease in the mean angle-of-attack $\overline{\alpha}$ to -12.5°, a wave phenomenon is becoming apparent over the aft portion of the lower or suction surface, analogous to the positive $\overline{\alpha}$ results. Also, a propagating wave now dominates the entire upper surface. With regard to the unsteady pressure magnitude, this decrease in the mean angle-of-attack has some effect near the leading edge, with the data-theory pressure difference correlation essentially unchanged and reasonable.

For the low solidity cambered airfoil vane row, the effect of steady loading on the unsteady fundamental-harmonic unsteady chordwise pressure and pressure difference responses are presented for increasing negative angles-of-attack in Figure 13. A comparison of the previously presented $\overline{\alpha} = +2.5°$ data with these $\overline{\alpha} = -2.5°$ results shows that there are only subtle differences in the upper and lower airfoil surface unsteady pressure magnitude data, with corresponding good unsteady pressure difference magnitude data-theory correlation. However, the phase angle distribution on the upper surface with $\overline{\alpha} = -2.5°$ exhibits a linear phase variation over the entire chord, a result far different from the $\overline{\alpha} = +2.5°$ data. Decreasing the mean angle-of-attack to $\overline{\alpha} = -7.5°$ affects the unsteady pressure magnitude over the front portion of the airfoil, with a noticeable effect on the lower surface phase angle. However,

there is no wave apparent on this lower airfoil surface, only the upper surface. Finally, decreasing $\overline{\alpha}$ to -12.5° results in wave phenomena over both the upper and lower airfoil surfaces. Note that with both airfoil surfaces dominated by wave phenomena, the unsteady pressure difference phase angle also exhibits a linear variation. This decrease in $\overline{\alpha}$ also affects the unsteady pressure magnitudes, primarily on the lower surface. Hence the poor unsteady pressure difference magnitude data-theory correlation.

Unsteady Lift

The effect of steady loading on the unsteady fundamental-harmonic lift coefficient is presented in Figure 14 for the low-solidity stator cascades. The symmetric-airfoil unsteady lift-coefficient magnitudes are in excellent agreement with linear theory for $-2.5° \leq \overline{\alpha} \leq +7.5°$. For the symmetric airfoils, the unsteady lift coefficient magnitude increases abruptly between $\overline{\alpha} = +7.5°$ and +12.5°, and then decreases for further increases in $\overline{\alpha}$. For the cambered airfoils, this abrupt increase and subsequent decrease in the unsteady lift coefficient magnitude is delayed until between $\overline{\alpha} = +12.5°$ and +17.5°. These abrupt increases coincide with the appearance of the wave phenomena on the upper airfoil surface and the increase in the upper surface unsteady pressure magnitude.

For negative mean angles-of-attack, the magnitude of the unsteady lift coefficient do not exhibit an abrupt change, although they decrease with increasingly negative values of the mean angle-of-attack. For the symmetric airfoils, this decrease occurs near $\overline{\alpha} = -7.5°$ where a wave was noted on the lower surface. For the cambered airfoils, the unsteady lift coefficient varies slightly with mean angle-of-attack for $\overline{\alpha}$ between -2.5° and -7.5°, corresponding to the existence of a wave on the upper surface, with a somewhat larger decrease in the unsteady lift at $\overline{\alpha} = -12.5°$ where waves were noted on both airfoil surfaces. Thus, the asymmetries previously noted for large positive and negative mean angles-of-attack are clearly evident.

For the high solidity symmetric airfoil vane row, the effect of steady loading on the unsteady flow fundamental-harmonic lift coefficient is presented in Figure 15. The unsteady lift-coefficient magnitudes correlate reasonably well with linear theory for $-2.5° \leq \overline{\alpha} \leq +7.5°$, although the data are increased in value. At $\overline{\alpha} = 12.5°$, the unsteady lift coefficient magnitude abruptly decreases, with a corresponding abrupt increase at $\overline{\alpha} = 17.5°$ and 22.5°. These correspond to the previously noted pressure magnitude change at $\overline{\alpha} = 12.5°$, the upper surface leading edge region wave at $\overline{\alpha} = 17.5°$ and the wave phenomena over the entire upper airfoil surface at $\overline{\alpha} = 22.5°$.

Comparing the high and low solidity unsteady lift coefficients shows that the angle-of-attack variations have less effect on the high-solidity responses, particularly for large positive $\overline{\alpha}$. Note the absence of the abrupt lift-coefficient magnitude increase at high positive $\overline{\alpha}$ in the high-solidity lift coefficients. Thus the steady-unsteady flow field interaction effects are less for high-solidity cascade because high-solidity cascade airfoils have lower steady loading distributions for the same $\overline{\alpha}$.

Unsteady Flow Asymmetries

Strong asymmetries were noted to exist in the unsteady flow generated vane response for increasing positive and negative angles-of-attack. This is a result of the unsteady loading cycle. Figure 16 depicts a large axial flow velocity for the free stream flow. In the wake region, the flow velocity decreases and the absolute flow angle increases to approximately 10°, as shown. When the wake region reaches airfoils set at time-averaged positive angles-of-attack, the instantaneous α increases as the flow velocity decreases. The increase in α and the decrease in inlet flow velocity have opposite effects on the instantaneous loading. The increase in α tends to increase the loading whereas the decrease in inlet flow velocity tends to decrease the loading. As the flow field changes from wake region back to free stream region, the decrease in α and increase in flow velocity have the reverse effect on the instantaneous loading. For airfoils set at time averaged negative angles-of-attack, the effects of α and flow velocity variations are additive. As the flow field changes from free stream to wake region, the instantaneous loading decreases because of the complementary effects of the decreasing α and flow velocity. The reverse occurs when the flow field changes from the wake region back to the free stream region. Thus, the loading cycles for airfoils set at time averaged positive angles-of-attack are very different from airfoils set at time-averaged negative angles-of-attack.

From another point of view, the asymmetry in the unsteady response behavior stems from the asymmetry in the unsteady flow field. Figure 6 clearly illustrates the unsteady flow field asymmetry by virtue of the gust propagation direction. Symmetric unsteady response behavior is not expected except for the case where the gust propagation direction and the mean downstream absolute flow velocity vector are aligned producing a pure transverse gust. For a pure transverse vortical gust, opposite airfoil surfaces would experience the same instantaneous loading for the opposite time-averaged angles-of-attack and the behavior of the unsteady response would not depend upon the sign of the angle-of-attack.

SUMMARY AND CONCLUSIONS

A series of experiments were performed to investigate the effect of blade row steady loading and separated flow on the vortical gust response of both low and high solidity vane rows, including the effects of airfoil camber. This was accomplished utilizing a unique single stage turbomachine research facility in which the flow is not generated by the blading but rather by an additional fan. This provided the ability to quantify the steady or mean performance of the stator row over a range of steady loading levels both with and without unsteady flow effects. In particular, for a specific stator mean angle-of-attack, the steady and mean stator aerodynamic performance were determined in a steady flow and also in an unsteady flow generated by a rotor at the same mean operating condition. This enabled the stator vane row dynamic stall conditions to be identified. The unsteady aerodynamic response of both symmetric and cambered stator vanes configured as low and high solidity stator vane rows was then investigated over a range of mean angles of attack.

Correlation of the steady and time-averaged lift revealed that the unsteady flow both increased the lift and also delayed stall

onset to larger mean angles-of-attack. Also, increased cascade solidity greatly reduced the slope of the lift coefficient, thereby greatly delaying stall onset in both steady and unsteady flow.

At low loading, $\overline{\alpha} = 2.5°$, unsteady fundamental-harmonic unsteady chordwise pressure and pressure difference responses of the symmetric airfoil cascades, both low and high solidity, and the low solidity cambered airfoils exhibit excellent data-theory correlation, with the effects of camber apparent in the low solidity cambered airfoil results.

For positive mean angles-of-attack, increased steady loading revealed the formation of a wave phenomenon on the suction surface. The wave was initially noted on the aft chord region, with the entire suction surface dominated by this wave as the mean angle-of-attack was further increased. Also, an increase in the unsteady lift magnitude on the upper surface accompanied this wave phenomenon. The first appearance of this wave was in good agreement with the first effects noted of the unsteady flow on the time-averaged lift. The convection velocity of this wave was a function of the solidity, propagating at about 50% of the free stream velocity for the low solidity symmetric or cambered airfoil vane rows, and at approximately free stream velocity for the high solidity cascade.

Strong asymmetries exist in the unsteady flow generated vane response for increasing positive and negative mean angles-of-attack, even for the symmetric airfoils. This is a result of the unsteady loading cycle. Also, at negative mean angles-of-attack, the upper surface, i.e., the pressure surface, exhibits a wave phenomenon, not the suction or lower surface as might have been expected. A further decrease in the mean angle-of-attack produces a wave phenomenon which is becoming apparent over the aft portion of the lower or suction surface, analogous to the positive $\overline{\alpha}$ results. Finally at large negative mean angles of attack, wave phenomena dominate the entire upper and lower airfoil surfaces. Thus, as the loading is increased, dynamic stall may be significant for turbomachines.

REFERENCES

Becker, H. A., and Brown, A. P. G., 1974, "Response of Probes in Turbulent Streams," *Journal of Fluid Mechanics*, Vol. 62, part 1, pp. 85-114

Henderson, G.H. and Fleeter, S., "Vortical Gust Response of a Low Solidity Vane Row Including Steady Loading and Dynamic Stall Effect," *ASME Paper 94-GT-295*, May 1994.

McCroskey, W.J., 1981, "The Phenomenon of Dynamic Stall," *NASA TM-81264.*

Reddy, T.S.R. and Mehmed, O., 1989, "Aeroelastic Analysis of Prop Fan Blades with a Semiempirical Dynamic Stall Model," *AIAA Paper 89-2685.*

Smith, S.N., 1972, "Discrete Frequency Sound Generation in Axial Flow Turbomachines," *ARC R & M 3709.*
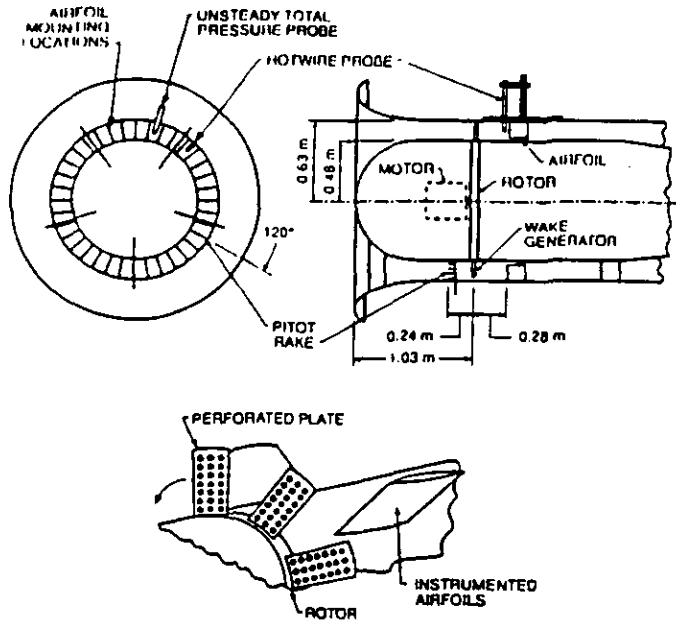
7

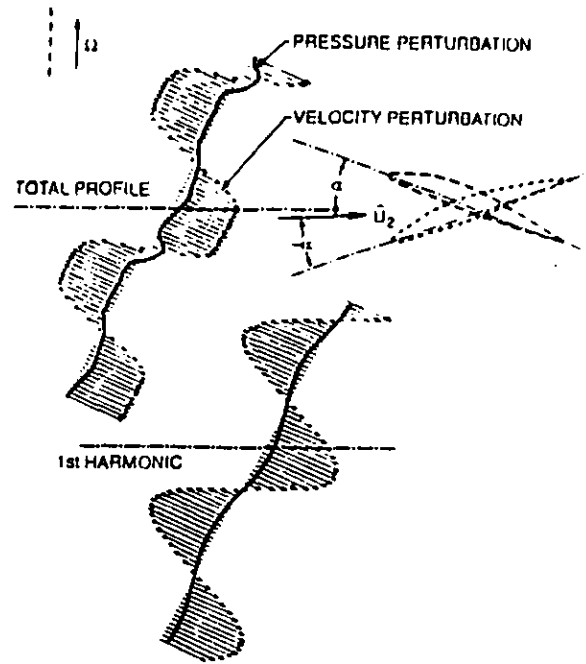Figure 1. Rotating annular cascade and perforated plate rotor wake generators

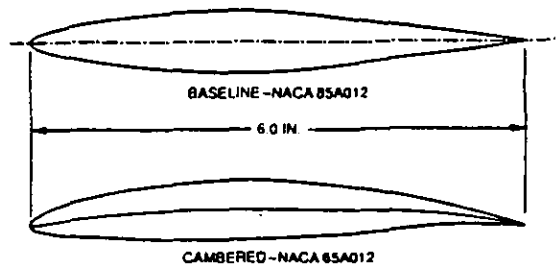Figure 3. Aerodynamic forcing function

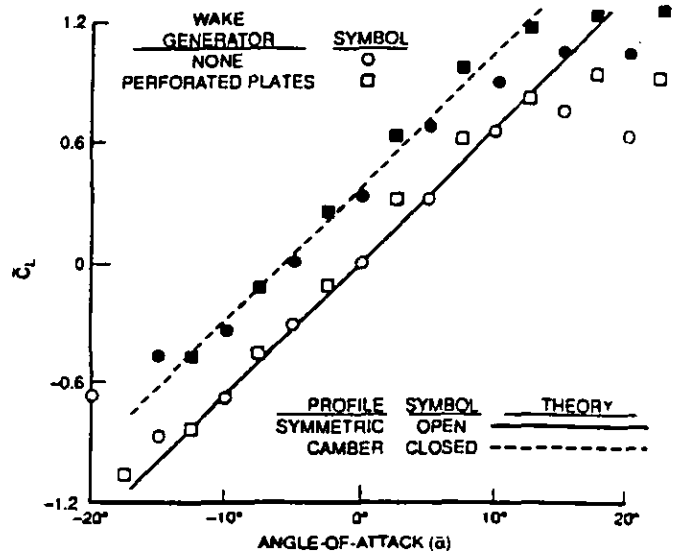

Figure 2. Instrumented stator airfoil profiles

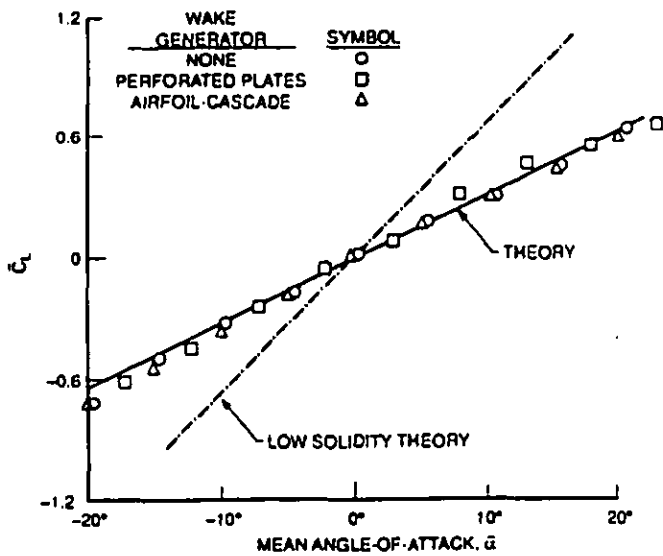Figure 4. Steady and time-averaged lift coefficients - low solidity cascades

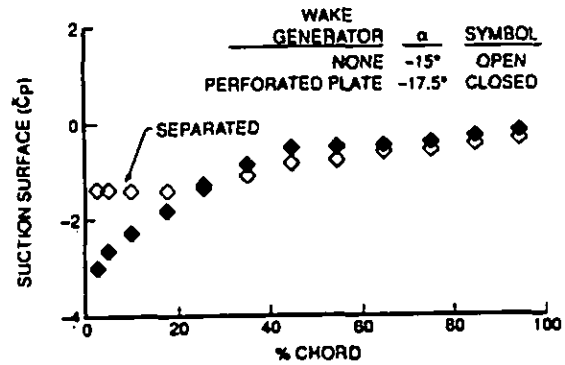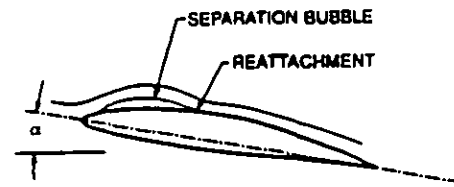Figure 5. Steady and time-averaged lift coefficients - high solidity cascade

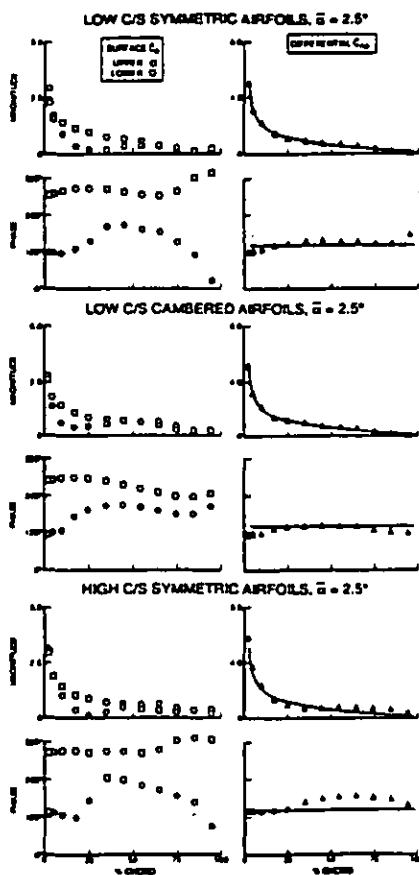Figure 6. Unsteady flow field effect on airfoil stall characteristics

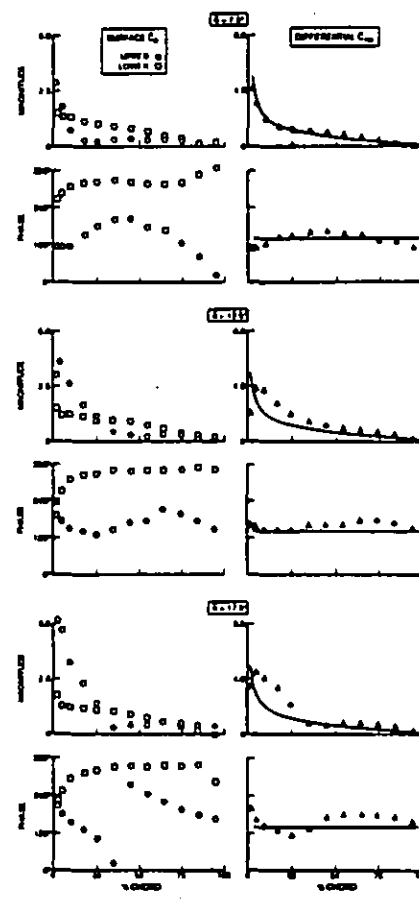Figure 7. Vortical gust response of low and high solidity vane rows at low loading

Figure 8. Steady loading effect on vortical gust response of the low solidity symmetric airfoil cascade - positive angles-of-attack

9
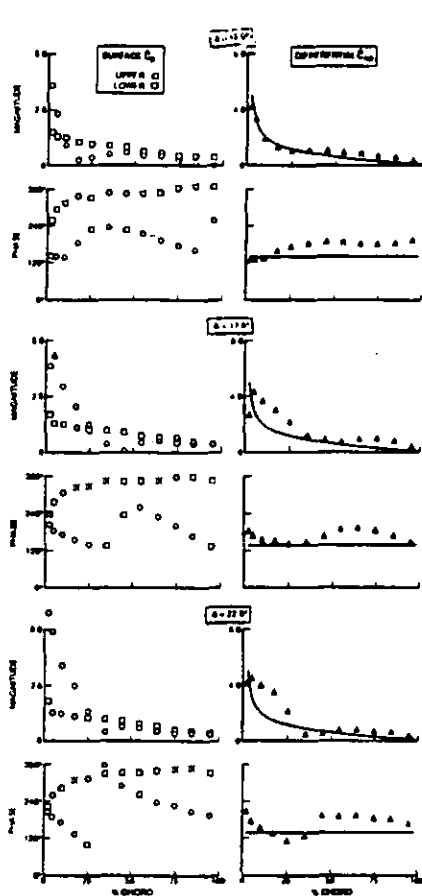
Figure 9. Steady loading effect on vortical gust response of the low solidity cambered airfoil cascade - positive angles-of-attack
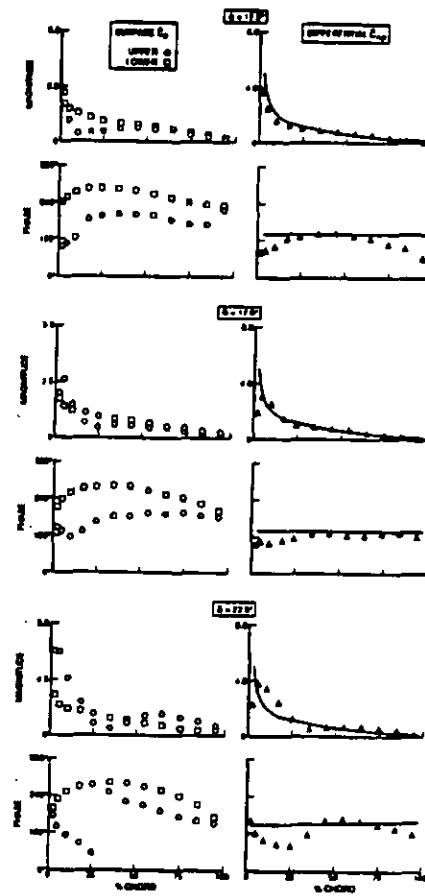
Figure 10. Steady loading effect on vortical gust response of the high solidity symmetric airfoil cascade - positive angles-of-attack
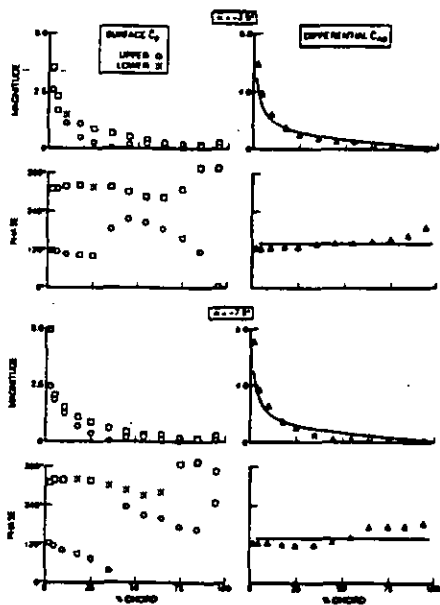
Figure 11. Steady loading effect on vortical gust response of the low solidity symmetric airfoil cascade - moderate negative angles-of-attack
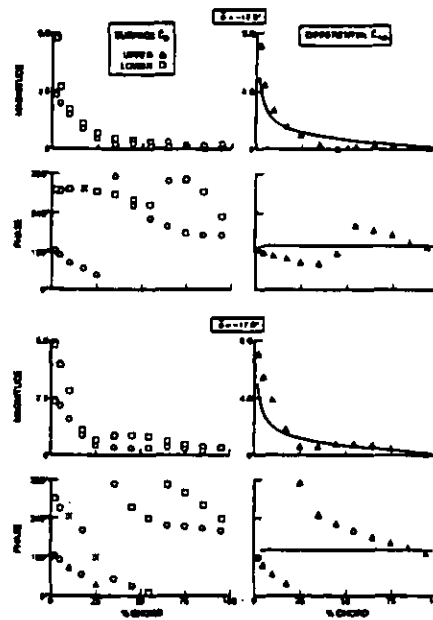
Figure 12. Steady loading effect on vortical gust response of the low solidity symmetric airfoil cascade - large negative angles-of-attack

10